



## Research article

# Formation of intraneuronal iron deposits following local release from nanostructured silica injected into rat brain parenchyma

E. Ortiz-Islas<sup>a</sup>, A.A. Ponce-Juárez<sup>b</sup>, F. Tzompantzi-Morales<sup>c</sup>,  
M.E. Manríquez-Ramírez<sup>d</sup>, C. Rubio<sup>e</sup>, M. Calvillo-Velasco<sup>f</sup>, G. Chávez-Cortés<sup>f</sup>,  
F. Missirlis<sup>g</sup>, M. Rubio-Osornio<sup>h,\*</sup>

<sup>a</sup> Laboratory of Molecular Neuropharmacology and Nanotechnology, National Institute of Neurology and Neurosurgery, Manuel Velasco Suarez. Insurgentes Sur 3877. Col. La Fama, 14269., Mexico City, Mexico

<sup>b</sup> Doctoral Program in Biomedical Sciences, National University Autonomous of Mexico. Universidad 3004, Copilco, Coyoacán, 04510, Mexico City, Mexico

<sup>c</sup> Metropolitan Autonomous University-Iztapalapa. Av. San Rafael Atlixco, Iztapalapa, 09340., Mexico City, Mexico

<sup>d</sup> ESIQIE-National Polytechnic Institute. Instituto Politécnico Nacional s/n, Col. Zacatenco, 07738, Mexico City, Mexico

<sup>e</sup> Neurophysiology Department, National Institute of Neurology and Neurosurgery, Manuel Velasco Suarez. Insurgentes Sur 3877. Col. La Fama, 14269., Mexico City, Mexico

<sup>f</sup> Experimental Laboratory of Neurodegenerative Diseases, National Institute of Neurology and Neurosurgery, Manuel Velasco Suarez. Insurgentes Sur 3877. Col. La Fama, 14269., Mexico City, Mexico

<sup>g</sup> Department of Physiology, Biophysics and Neuroscience, Cinvestav. Avenida Instituto Politécnico Nacional 2508, San Pedro Zacatenco, Gustavo A. Madero, 07360., Mexico City, Mexico

<sup>h</sup> Neurochemistry Department, National Institute of Neurology and Neurosurgery, Manuel Velasco Suarez. Insurgentes Sur 3877. Col. La Fama, 14269., Mexico City, Mexico

## ARTICLE INFO

## Keywords:

Nanostructured SiO<sub>2</sub>  
SiO<sub>2</sub>-Fe  
Iron  
Parkinson's disease

## ABSTRACT

Nanostructured materials with controllable properties have been used to cage and release various types of compounds. In the present study, iron-loaded nanostructured sol-gel SiO<sub>2</sub>-Fe materials were prepared and injected into the rat brain to develop a method for gradual iron delivery into the neurons with the aims to avoid acute iron toxicity and develop an animal model of gradual, metal-induced neurodegeneration. Nanoparticles were prepared by the traditional method of hydrolysis and condensation reactions of tetraethyl orthosilicate at room temperature and subsequent heat treatment at 200 °C. FeSO<sub>4</sub> was added *in situ* during the silica preparation. The resulting materials were characterized by UV-VIS and infrared spectroscopies, X-ray diffraction, and N<sub>2</sub> adsorption-desorption. An *in vitro* ferrous sulfate release test was carried out in artificial cerebrospinal fluid as the release medium showing successful ferrous sulfate loading on nanostructured silica and sustained iron release during the test time of 10 h. Male Wistar rats administered with SiO<sub>2</sub>-Fe nanoparticles in the *substantia nigra pars compacta* (SNpc) showed significant intraneuronal increase of iron, in contrast to the animals administered with FeSO<sub>4</sub> that showed severe neuronal loss, 72 h post-treatment. Both treatments induced lipid fluorescent product formation in the ventral midbrain, in contrast to iron-free SiO<sub>2</sub> and PBS-only injection controls. Circling behavior was evaluated six days after the intranigral microinjection, considered as a behavioral end-point of brain damage. The apomorphine-induced ipsilateral turns in the

\* Corresponding author. Neurochemistry Department National Institute of Neurology and Neurosurgery Ave. Insurgentes Sur No. 3877, Col. La Fama Mexico City P.C., 14269, Mexico.

E-mail address: [moises.rubio@innn.edu.mx](mailto:moises.rubio@innn.edu.mx) (M. Rubio-Osornio).

<https://doi.org/10.1016/j.heliyon.2024.e27786>

Received 7 July 2023; Received in revised form 6 March 2024; Accepted 6 March 2024

Available online 14 March 2024

2405-8440/© 2024 Published by Elsevier Ltd.

This is an open access article under the CC BY-NC-ND license

(<http://creativecommons.org/licenses/by-nc-nd/4.0/>).

treated animals presented significant differences in relation to the control groups, with  $\text{FeSO}_4$  administration leading to a dramatic phenotype, compared to a milder impact in  $\text{SiO}_2$ -Fe administrated animals. Thus, the use of  $\text{SiO}_2$ -Fe nanoparticles represents a slow iron release system useful to model the gradual iron-accumulation process observed in the *SNpc* of patients with idiopathic Parkinson's disease.

## 1. Introduction

The use of local drug delivery systems through carrier materials with sizes between 1 and 100 nm has increased substantially with the application of nanotechnology in pharmaceutical industry. Silicon dioxide ( $\text{SiO}_2$ ), also known as silica, has properties allowing a wide range of applications in energy source, electronic, sensor, and catalytic processes [1]. Several methods exist to obtain synthetic silica of nanometric sizes with controllable properties such as crystallinity, porosity, shape, and biocompatibility [2–4]. Sol-gel technology is one such method, widely used to get silica because it allows synthesis at low temperatures [5,6]. The sol-gel route consists of hydrolysis and condensation of tetraethyl orthosilicate (TEOS) in acid, basic or neutral conditions [7]. Resulting silica materials contain porous structures and high surface area, where diverse molecules can be hosted, even when added in parallel to the silica synthesis procedure. The structural properties of silica nanoparticles are significant in biomedical applications, such as imaging, disease detection, drug delivery, disease monitoring, and ablative therapies [8–14]. Specifically, the amorphous-porous silica structure can concentrate drugs, later released over a prolonged time [10,15–18]. Drug delivery nanotechnologies have substantially changed because of the human body's complexity, which sets specialized demands for the treatment of diseases that affect specific organ systems that require the drug to act locally. Since many drugs provoke unwanted side effects in healthy tissues, nanotechnology aims for the treatment substance to only interact with its target in the damaged area. Simultaneously, controlled release of the drug is another advantage that prevents secondary effects [19]. Amongst different types of nanocarriers used in the biomedical field, mesoporous materials have emerged as an innovative tool and amorphous silica is a promising platform for the development of controlled drug delivery matrices.

On the other hand, Parkinson's disease (PD) is a neurodegenerative disorder, in which, and despite advances in understanding the neurochemical processes underlying behavioral alterations in PD, the causes of the first changes that initiate neuronal degeneration are still unknown [20]. Amongst the proposed causal factors involved in the neuronal death of the *substantia nigra pars compacta* (*SNpc*) are iron deposits, mitochondrial dysfunction, free radical overproduction, and oxidative stress [21]. Ventral midbrain iron deposits are evaluated through brain parenchyma sonography of clinically diagnosed idiopathic PD, showing that iron is a marker with 96% of specificity and 91% of sensitivity [22]. However, until now, no experimental model of PD exists, arising from iron accumulation in the *SNpc* as a primary cause and the neurochemical and molecular mechanisms that lead to intraneuronal iron accumulation in the rat *SNpc* are not yet fully understood.

In the present work, a nanostructured and biocompatible  $\text{SiO}_2$  matrix loaded with  $\text{FeSO}_4$  has been synthesized and characterized to obtain a gradual and sustained iron release system. The  $\text{SiO}_2$ -Fe matrix has been generated to reproduce intraneuronal iron accumulation in the midbrain of rats and induce one of the most important markers of neuronal damage observed in the *SNpc* of patients with idiopathic PD: the iron deposits.

## 2. Materials and methods

### 2.1. Chemical substances

Ferrous sulfate ( $\text{FeSO}_4$ ) (Sigma-F8263), deionized water, tetraethyl orthosilicate (TEOS) (Sigma-Aldrich, 98%), ammonium sulfate (Sigma-A3678), ethanol (Grupo Internacional ICR, 99.5%).

### 2.2. $\text{SiO}_2$ and $\text{SiO}_2$ -Fe sample preparation

Nanostructured silica was prepared based on the method reported by Parameswaran et al. [23]. Ferrous sulfate was added during the TEOS hydrolysis step. Molar ratios used were TEOS/ $\text{H}_2\text{O}$ :1/16, and TEOS/ethanol:1/8. 0.5% and 10% (weight) of ammonium sulfate and ferrous sulfate silica were used, respectively. The procedure described below was followed.

#### 2.2.1. $\text{SiO}_2$

0.05 g of ammonium sulfate was dissolved in 100 mL of water, keeping the solution stirred for 30 min. A mixture of 84 mL ethanol and 37.5 mL TEOS was added slowly (approximately 5 h). The final mixture was kept stirring until gel formation. Then, excess water and alcohol were removed, and the obtained powder was dried at 70 °C for 12 h. Finally, the sample was thermally treated at 200 °C.

#### 2.2.2. $\text{FeSO}_4/\text{SiO}_2$

0.05 g of ammonium sulfate and 100 mL of water were mixed under stirring for 30 min. A mixture of 37.5 mL TEOS and 84 mL ethanol was added slowly for 5 h. Once TEOS addition had been completed, the solution was stirred for another 2 h. Afterwards, 1 g of ferrous sulfate freshly dissolved in 60 mL of water was added and the final mixture was stirred until the gel formed. Water and alcohol

were removed, and the obtained powder was dried at 70 °C for 12 h.

### 2.3. Sample characterization

#### 2.3.1. Scanning electron microscopy (SEM)

Sample morphology, surface texture, and elemental analysis were analyzed using a Field Emission Scanning Electron Microscope (Schottky JSM-7800 F). Samples were imaged using a secondary electron detector at an acceleration voltage of 2.0 kV under an ultra-high vacuum. Sample dimensions were measured with the ImageJ software.

#### 2.3.2. Ultraviolet–visible spectroscopy

The powder samples' diffuse reflectance spectra were obtained using a Cary 100 UV–Vis spectrophotometer equipped with an integrating sphere and BaSO<sub>4</sub> as a baseline reference. Each spectrum was taken in a 190–900 nm wavelength interval.

#### 2.3.3. Infrared spectroscopy

198 mg of KBr and 2 mg of each sample were mixed and ground to be compressed until a translucent wafer was formed. The wafers were immediately dried at 100 °C for 24 h to remove environmental moisture. After, the wafers were analyzed in an IRAffinity Shimadzu spectrophotometer in a 5000–500 cm<sup>-1</sup> wavenumber interval and a resolution of 8 cm<sup>-1</sup>.

#### 2.3.4. X-ray diffraction

The sample holder was filled with the corresponding sample to form a uniform surface. Subsequently, the holder was introduced to a Bruker D2 Phaser diffractometer, which uses Cu K $\alpha$  radiation ( $\lambda = 1.5405$  nm), and a rate analysis of 0.6°/sec.

#### 2.3.5. N<sub>2</sub> adsorption-desorption measurements

N<sub>2</sub> adsorption-desorption isotherms were obtained to quantify the specific surface area ( $S_{BET}$ ) using the BET method and the pore volume ( $V_p$ ) and pore diameter ( $D_p$ ) using the BJH method. Samples were pretreated with a vacuum at 70 °C for 12 h. After that, adsorption-desorption measurements were performed at liquid nitrogen temperature (77 K) in a Belsorp II gas adsorption apparatus over a relative pressure range of 0.01–0.99 P/P<sub>0</sub>.

#### 2.3.6. Thermogravimetric analysis

Thermograms of thermogravimetric analysis (TGA) of the samples were obtained using a Setaram Labsys Evo apparatus. The temperature range analyzed was from room temperature to 800 °C, with a ramp of 10 °C/min and under a flow of 60 mL of N<sub>2</sub>.

### 2.4. In vitro ferrous sulfate release test

Simulated cerebrospinal fluid (SCF) was used as a release medium and was prepared according to the information reported by Düzli et al. [24]. Approximately 5–10 mg of each FeSO<sub>4</sub>/SiO<sub>2</sub> sample was slightly pressed to form a small cylinder, which was added to 20 mL of SCF. At predetermined times an aliquot of 3 mL was removed from the release medium for its measurement by UV spectroscopy in an Agilent Cary 60 spectrophotometer. After each measure, the aliquot was returned to the original release medium. Each time the iron concentration was obtained using a previously built calibration curve plotted of solutions of FeSO<sub>4</sub> concentrations, versus maximum absorbance at 205 nm for each solution. The experiment was performed in triplicate.

### 2.5. Animal experimental stage

Adult male Wistar rats (300–330 g) were used throughout the study. Animals were provided by the animal research facilities at the Institute of Cellular Physiology at the National Autonomous University of Mexico. The use of animals was performed according to official regulatory guides regarding laboratory animal use and care (NOM-62-ZOO-2001). The animals were housed in acrylic box cages and placed under constant conditions of temperature, humidity, and light (12 h light/dark cycles) and provided with a standard commercial rat chow diet and water *ad libitum*. Before the microinjection, the animals were intraperitoneally administrated a mixture of ketamine/xylazine anesthesia (80/12 mg/kg). 3–5 min later, the animals were administrated under stereotaxic coordinates: -5.4 mm later to bregma, -2.0 mm lateral to the midline, and -7.8 mm ventral to the dura in the right SNpc, according to the stereotaxic Paxinos and Watson atlas [25]. The experimental group was dosed with a single unilateral intranigral (i.n.) 20  $\mu$ g injection of SiO<sub>2</sub>-Fe nanoparticle in 2  $\mu$ L of PBS as vehicle solution; 2  $\mu$ L of PBS was injected to the control group, while another group was administrated with 20  $\mu$ g of SiO<sub>2</sub> as a control group for evaluating nanostructured materials effect; and finally, the last group was administered with 800 ng of FeSO<sub>4</sub> in 2  $\mu$ L of PBS, iron equivalent concentration to the concentration used in the group administered with 20  $\mu$ g of SiO<sub>2</sub>-Fe.

### 2.6. Histological analysis with the prussian blue technique

72 h after stereotaxic microinjection, rats belonging to the different groups (n = 3–4) were anesthetized and perfused with 200 mL of saline solution and followed by 200 mL of 4% paraformaldehyde. The brains were removed and postfixed in the same fixative solution for 24 h, and later embedded in sucrose solution to 15% during 24 h; finally, the brains were incubated in sucrose solution to

30% till their utilization. 25- $\mu\text{m}$  thick coronal sections (Leica CM 1520 cryostat) were taken from each brain at the midbrain area level, about  $-4.6$  to  $-6.0$  mm from bregma. The intraneuronal iron deposits were evaluated with the Prussian blue stain (Perls technique). The sections were immersed in a 10% potassium ferrocyanide solution (J.T. Baker 3104-01) plus a 20% hydrochloric acid solution (J.T. Baker 9535-05) in equal parts for 1 h, followed by a wash with distilled water and immersion in a nuclear fast red solution for 30 min. Then, the sections were washed with water and dehydrated with gradual alcohols, cleared with xylol, for later mounting with resin (Permount, Fisher Chemical SP15-500). Photomicrographs were obtained with the IM1000 program of Leica Microscope with a 40X objective. Iron positive (blue) cells were counted in the different treatments: PBS,  $\text{SiO}_2$ ,  $\text{FeSO}_4$ , and  $\text{SiO}_2$ -Fe from 5 sequential sections of 5 slides per rat, selected randomly.

## 2.7. Lipid peroxidation assay

Lipid fluorescent product determination was performed in the rat *SNpc* ( $n = 5-7$ ) 72 h after the  $\text{SiO}_2$ -Fe administration. Striatal tissue was homogenized in sterile saline (2.2 mL). 1 mL of the homogenate was then mixed with 4 mL chloroform-methanol mixture (2:1, v/v) [26]. Tubes were capped and vortexed for 10 s and the mixture was ice-cooled for 30 min to allow phase separation. The aqueous phase was discarded and 1 mL of the chloroformic layer transferred into a quartz cuvette, to which 150  $\mu\text{L}$  of methanol were added. Fluorescence was measured in a PerkinElmer LS50B luminescence spectrophotometer at 370 nm excitation and 430 nm emission. Protein content was measured in samples according to the method described by Lowry et al. (1951) [27]. Results were expressed as arbitrary fluorescence units/ $\mu\text{g}$  of protein.

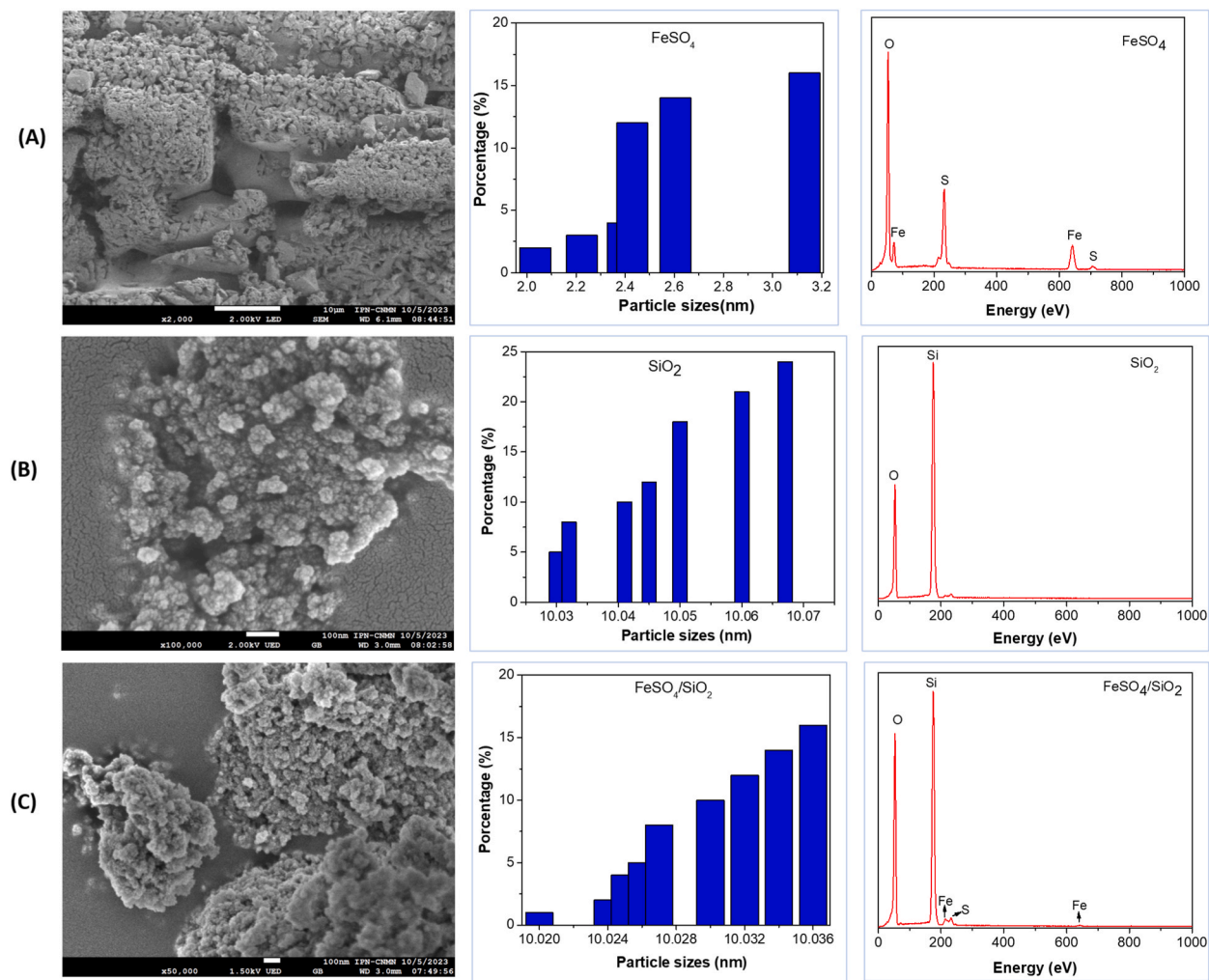


**Fig. 1.** SEM images, histograms the particle size distribution and EDS graphics of (A)  $\text{FeSO}_4$ , (B)  $\text{SiO}_2$ , and (C)  $\text{SiO}_2$ -Fe samples. Scale bar values: (a) 10  $\mu\text{m}$ , (b) 100 nm, and (c) 100 nm.

## 2.8. Animal behavior test

Apomorphine-induced circling behavior was assessed in rats ( $n = 7$ ) as previously described [28]. Six days following the microinjection, animals were treated subcutaneously with a mixture of apomorphine (1 mg/kg) and ascorbic acid (1 mg/kg) and then placed into individual box cages. Five minutes later, the number of rotations was recorded for 1 h. Rotations were considered as  $360^\circ$  turns. In this assay, we evaluated the number of rotations as a marker of the level of iron-induced damage. Results were expressed as the total number of turns in 1 h period (turns/h).

## 2.9. Statistics

Prussian blue staining results were analyzed by one-way ANOVA followed by Tukey's multiple comparison test. Results from lipid fluorescent products were analyzed by one-way ANOVA followed by Dunnett's multiple comparisons test. Data obtained from evaluating circling behavior were analyzed by Kruskal-Wallis' followed by Dunn's test. Statistical significance was set at  $P < 0.05$ .

## 3. Results

### 3.1. Nanostructured $\text{SiO}_2$ materials characterization

#### 3.1.1. Scanning electron microscopy

Fig. 1 shows the SEM images, **particle size distribution histograms**, and energy dispersive spectroscopy (EDS) plots of  $\text{FeSO}_4$ ,  $\text{SiO}_2$ , and  $\text{SiO}_2\text{-Fe}$  samples. From the SEM image of  $\text{FeSO}_4$ , it is possible to identify orthogonal structures greater than  $10\ \mu\text{m}$ ,

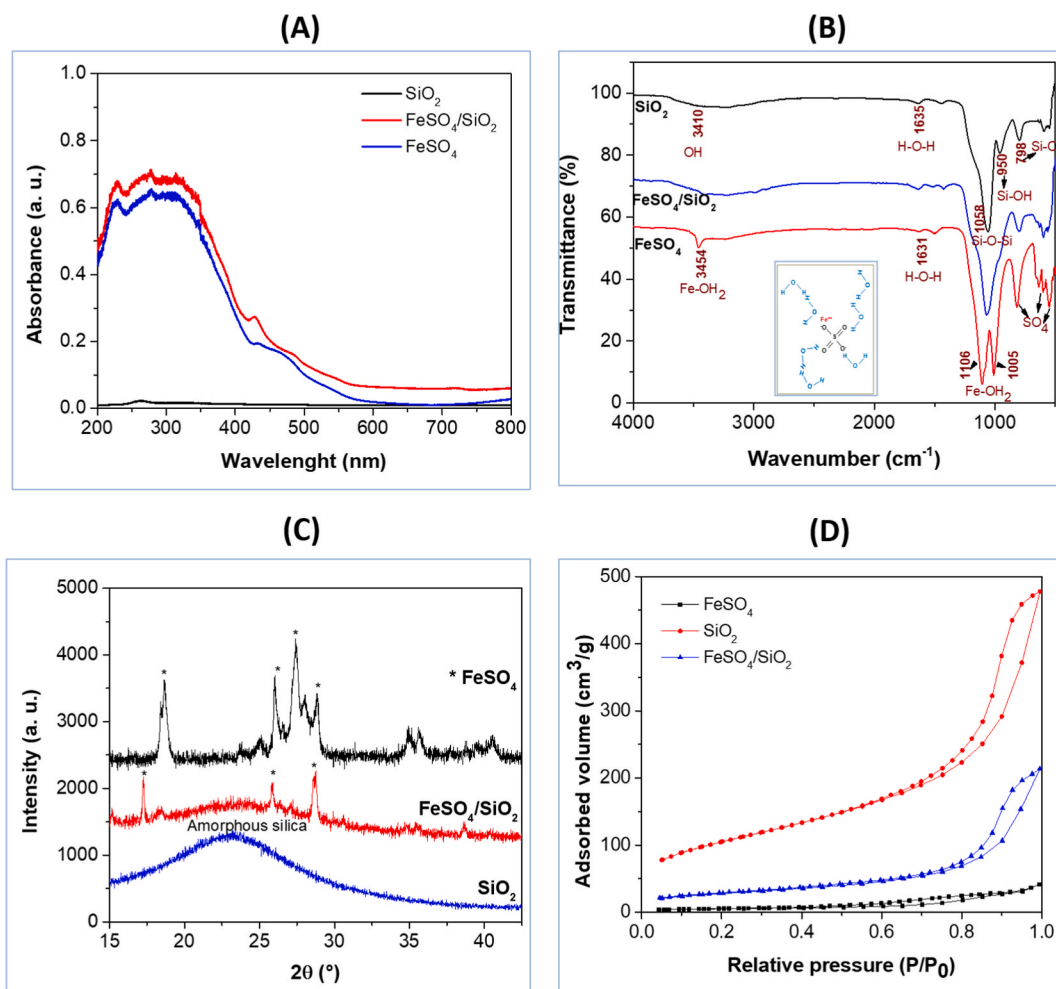


**Fig. 2.** (A) Diffuse reflectance UV-Vis spectra in solid state, (B) FTIR spectra, (C) X-ray diffraction patterns, and (d)  $\text{N}_2$  adsorption-desorption isotherms of the  $\text{FeSO}_4$ ,  $\text{SiO}_2$ , and  $\text{SiO}_2\text{-Fe}$  samples.

themselves constituted of smaller orthogonal/square particles (Fig. 1A). Particle size distributions are presented as a histogram insert within the SEM image that shows a substantial percentage of particles ranging between 2.4 and 3.2 nm (Fig. 1A). As expected, the EDS spectrum of FeSO<sub>4</sub> shows the presence of iron, oxygen, and sulfur in a percentage of 33, 50, and 18 wt %, respectively (Fig. 1A). In contrast, the SEM image for silica revealed aggregates of nanoparticles with sizes of approximately 100 nm (Fig. 1B). These aggregates, in turn, are formed from smaller spherical nanoparticles of about 10 nm in size (as shown in the respective histogram). It is possible to observe the porous nanostructured network generated. The SiO<sub>2</sub> EDS spectrum shows the presence of silicon and oxygen atoms, as expected, in a percentage of 43 and 57 wt %, respectively (Fig. 1B). Last, the SEM image corresponding to the SiO<sub>2</sub>-Fe sample also consists of nanoparticle aggregates but there are larger than the silica sample, exceeding the 100 nm scale (Fig. 1C). However, these aggregates are also formed from nanoparticles with sizes of 10 nm and similar to the SiO<sub>2</sub> sample, a porous network formation can also be observed in the SiO<sub>2</sub>-Fe sample. The EDS spectrum for the SiO<sub>2</sub>-Fe sample shows the presence of silicon, oxygen, iron, and sulfur in 42, 55, 1, and 2 wt %, respectively (Fig. 1C).

### 3.1.2. UV-vis spectroscopy

Fig. 2A shows the solid-state samples' UV-Vis spectra. The FeSO<sub>4</sub> spectrum contains two significant absorptions, the first observed at 424–570 nm corresponds to electronic transitions from the sulfate ion to the iron atom, while the second that appears below 424 nm corresponds to electronic transitions in the *d* orbitals of the iron atoms. These absorptions were also observed in the SiO<sub>2</sub>-Fe sample, in contrast to SiO<sub>2</sub>, which did not show absorption in the UV-Vis range above background level. These results suggest ferrous sulfate was occluded in silica without undergoing structural changes.

### 3.1.3. FTIR spectroscopy

Fig. 2B displays the Fourier transformed infrared (FTIR) spectra of the FeSO<sub>4</sub>, SiO<sub>2</sub>, and SiO<sub>2</sub>-Fe solids. The chemical structure of FeSO<sub>4</sub>·7H<sub>2</sub>O used in this study is also drawn in the inset of Fig. 2B. The FeSO<sub>4</sub> spectrum contains several bands related principally to hydroxyl (OH<sup>-</sup>) and SO<sub>4</sub><sup>-</sup> ions. The high-frequency region at 3454 cm<sup>-1</sup> is a signal associated with νOH stretching vibration from the water molecules interacting with iron atoms and sulfate ions. The band located at 1631 cm<sup>-1</sup> is related to bending vibrations from water molecules. The νSO<sub>4</sub> band that appears at 1005 cm<sup>-1</sup>, and the band at 1106 cm<sup>-1</sup> are related to both sulfate ions and Fe-OH<sub>2</sub> species. Other bands at low frequencies 814, 630, 600, and 541 cm<sup>-1</sup> are also related to different vibrations modes of SO<sub>4</sub><sup>-</sup> ions. The SiO<sub>2</sub> spectrum, on the other hand, shows the characteristic signals of silica. The OH<sup>-</sup> band at 3410 cm<sup>-1</sup>, the NH band from ammonium sulfate at 3222 cm<sup>-1</sup>, the water band at 1635 cm<sup>-1</sup>, the characteristic Si-O-Si band from the silica network at 1058 cm<sup>-1</sup>, the band of Si-OH associated with Si-O-H bending vibrations at 950 cm<sup>-1</sup>, and the Si-O bending vibrations band at 798 cm<sup>-1</sup> were found in this sample. Several bands corresponding to sulfate ions are also readily observed since ammonium sulfate was used to functionalize the silica surface. Last, the SiO<sub>2</sub>-Fe sample shows all the signals corresponding to ferrous sulfate as well as those attributed to the silica. These results agree with the UV-Vis spectroscopic results that the ferrous sulfate did not undergo any structural change upon its occlusion in the silica nanoparticles.

### 3.1.4. X-ray diffraction

The X-ray diffraction patterns of FeSO<sub>4</sub>, SiO<sub>2</sub>, and SiO<sub>2</sub>-Fe samples are shown in Fig. 2C. The sulfate ferrous X-ray diffraction pattern shows several fine peaks at 18–30° that feature the ferrous compound. In contrast, the silica X-ray diffraction pattern consists of broadband characterized by amorphous silica. As expected, the SiO<sub>2</sub>-Fe diffraction pattern is a mixture of signals from ferrous sulfate and amorphous silica.

### 3.1.5. N<sub>2</sub> adsorption-desorption measurements

Fig. 2D reports the N<sub>2</sub> adsorption-desorption isotherms of the samples under study. The isotherm of FeSO<sub>4</sub> is characteristic of microporous or no porous materials, expected since the ferrous sulfate has a crystalline structure (Fig. 2C) and does not have porosity. In contrast, according to the IUPAC classification, the SiO<sub>2</sub> isotherm corresponds to a type IV, indicating that silica has a mesoporous structure. The isotherm of SiO<sub>2</sub>-Fe is similar to the silica sample because silica is the matrix. It is in a higher percentage, the difference being that N<sub>2</sub> was adsorbed at the porous structure, indicating that a portion of pores was occupied for the ferrous sulfate.

The surface area for ferrous sulfate is shallow at 17.88 m<sup>2</sup>/g, due to it being a crystalline sample. In contrast, the silica sample had a higher surface area of 358.7 m<sup>2</sup>/g since it is amorphous generating high porosity. The surface area of the SiO<sub>2</sub>-Fe sample decreased to 98.14 m<sup>2</sup>/g in comparison with the silica sample. This decrease is due to ferrous sulfate occupying part of the surface area. Table 1 summarizes the textural properties of all samples, where it is possible to observe that the pore volume decreased from silica to SiO<sub>2</sub>-Fe, due to these pores being partially filled with the ferrous sulfate molecules.

**Table 1**  
Surface area (*S*<sub>BET</sub>), pore diameter (*D*<sub>p</sub>), and pore volume (*V*<sub>p</sub>) of the FeSO<sub>4</sub>, SiO<sub>2</sub>, and FeSO<sub>4</sub>/SiO<sub>2</sub> samples.

Sample	<i>S</i> <sub>BET</sub> (m <sup>2</sup> /g)	<i>D</i> <sub>p</sub> (nm)	<i>V</i> <sub>p</sub> (cm <sup>3</sup> /g)
FeSO <sub>4</sub>	17.88	30.48	0.064
SiO <sub>2</sub>	358.7	35.03	0.746
FeSO <sub>4</sub> /SiO <sub>2</sub>	98.14	40.66	0.330

### 3.1.6. Thermogravimetric analysis

The TGA pattern of  $\text{SiO}_2$  and  $\text{SiO}_2$ -Fe samples is depicted in Fig. 3. It is possible to observe two crucial weight losses from the silica thermogram. The first is seen below  $150^\circ\text{C}$ , corresponding to water and ethanol evaporation used in the silica synthesis. A weight loss of 10% at  $150^\circ\text{C}$  was observed. The second weight loss is seen in the range of  $150$ – $800^\circ\text{C}$ , which corresponds to total dehydration and surface dehydroxylation of the silica sample. The weight loss in this range was 10%. The TGA thermogram of the  $\text{SiO}_2$ -Fe sample shows instead four crucial weight losses. The weight loss seen at  $150^\circ\text{C}$  is due to the elimination of water and ethanol in the synthesis procedure. However, it also includes the water molecules in the ferrous salt, which is transformed from  $\text{FeSO}_4 \cdot 7\text{H}_2\text{O}$  to  $\text{FeSO}_4 \cdot 4\text{H}_2\text{O}$  [29]. The weight loss seen at  $350^\circ\text{C}$  corresponds to the total dehydration of silica but also to the second loss of three water molecules from  $\text{FeSO}_4 \cdot 4\text{H}_2\text{O}$  to  $\text{FeSO}_4 \cdot \text{H}_2\text{O}$  in agreement with the literature [29]. The loss seen below  $545^\circ\text{C}$  corresponds to surface dehydroxylation of the silica sample and is also due to the dehydration of  $\text{FeSO}_4 \cdot \text{H}_2\text{O}$ . The final significant weight loss between  $545$  and  $800^\circ\text{C}$  corresponds to sulfate decomposition from the oxidation and dehydration of  $\text{FeSO}_4 \cdot \text{H}_2\text{O}$ . This sample had a total weight loss of 42%. These results are also consistent with the conclusion that the  $\text{FeSO}_4$  salt did not undergo any structural changes upon its incorporation in the silica nanoparticles resulting in the functionalized  $\text{SiO}_4$ -Fe matrix.

### 3.2. In vitro ferrous sulfate release results

Fig. 4A shows the  $\text{FeSO}_4$  release profiles as a time function of three independently performed tests. All three release profiles follow the same behavior, where a sustained release of ferrous sulfate is observed during the time the test lasted. Fig. 4B shows the average release profile with a lineal tendency. To determine the theoretical release mechanism of iron sulfate, the experimental data were fitted with several theoretical-mathematical models such as zero-order kinetics, first-order kinetics, Higuchi model, Hixson-Crowell model, and Korsmeyer-Peppas model [30]. The linear regression coefficient ( $R^2$ ) is the indicator for choosing the most probable release mechanism. The value of  $R^2$  must be as close as possible to 1 so that the mathematical model is selected and allows us to determine the theoretical release mechanism. Table 2 shows the profitability coefficients obtained for each mathematical model and the simplified linear equation of each model. The model with an  $R^2$  closest to 1 is that of Higuchi, who describes the release of drugs from insoluble matrices. This model explains that the drug release is can be by diffusion and dissolution. Therefore, the release mechanism in our system occurs by an initial dissolution of  $\text{FeSO}_4$  in contact with the liquid medium to diffuse through the pores to reach the release medium.

### 3.3. Histology

Next, we injected the  $\text{SiO}_2$  and  $\text{SiO}_2$ -Fe nanoparticles, along with respective phosphate buffered saline (PBS) and  $\text{FeSO}_4$  controls, into rat brains aiming for an initial characterization of their utility as a slow-release iron delivery system. Animals were sacrificed 72 h post-injection and their brains were dissected and sectioned. The use of Prussian blue staining in the group of animals microinjected intranigrally with vehicle solution ( $2\ \mu\text{L}$  of PBS) revealed tissue integrity without structural or cellular alterations, and no positive iron signals were observed (Fig. 5A). The group of animals administered with nanostructured materials of  $\text{SiO}_2$  did not show positive staining for iron, nor cellular or tissue alterations (Fig. 5B). The histological analysis by Prussian blue staining was only positive in the groups of animals administered intranigrally with the  $\text{FeSO}_4$  and nanostructured  $\text{SiO}_2$ -Fe material (Fig. 5C and D), albeit with significantly more intracellular iron present in the  $\text{SiO}_2$ -Fe treatment group. The nigral tissue of animals treated with  $\text{FeSO}_4$ , on the other hand, showed a severe alteration of tissue structure and neuronal degeneration, loss of tissue and loss of cellular structure with the presence of pyknotic nuclei, evidence of numerous cell loss (Fig. 5C). In contrast, when microinjected nanostructured  $\text{SiO}_2$ -Fe material, only intracellular deposits of iron formation were observed without apparent signs of large scale neurodegeneration

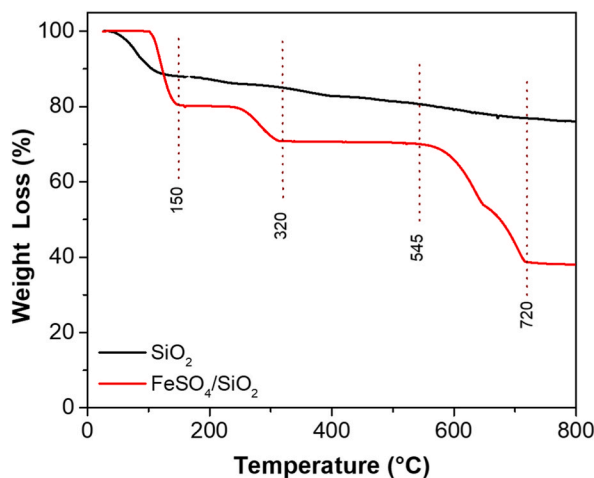


Fig. 3. TGA Thermograms of  $\text{SiO}_2$  and  $\text{SiO}_2$ -Fe samples.

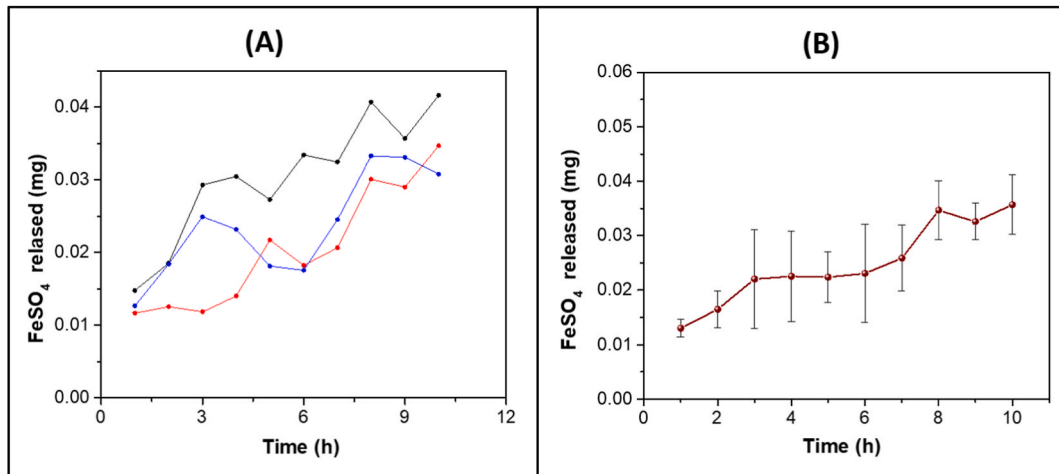


Fig. 4. (A) *In vitro* FeSO<sub>4</sub> release profiles from independent assays and (B) the averaged FeSO<sub>4</sub> release profile.

Table 2

Correlation coefficients R<sup>2</sup> obtained from the linear regression applied to the different mathematical models for the FeSO<sub>4</sub>/SiO<sub>2</sub> system.

Mathematical mode	Equation	R <sup>2</sup>
Zero order	$C_t = C_0 + K_0 t$	0.9484
First order	$\text{Log } C_0 = \text{Log } C_t - K_1 t / 2.303$	0.719
Higuchi	$Q = KH \times t^{1/2}$	0.9913
Korsmeyer-Peppas	$\text{Log } C_t = \text{log } K_{kp} + n \text{log } t$	0.7621
Hixson-Crowell	$C_0^{1/3} - C_t^{1/3} = K_{HCT}$	0.8567

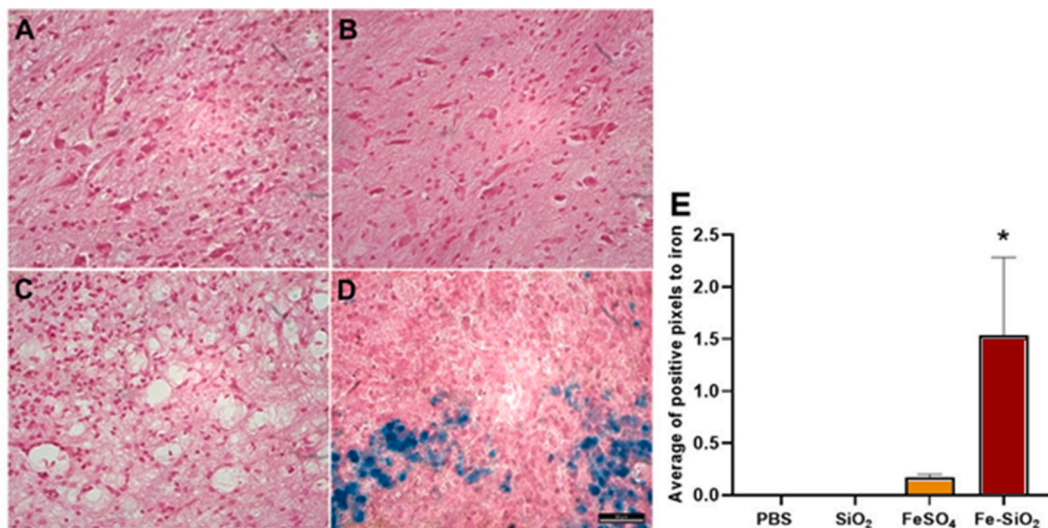


Fig. 5. Histological analyses of nanostructured materials administration effect. Each of the figures in the panel is representative of different groups (n = 3–4). A) Control group was administered with PBS and B) Group treated with 20  $\mu\text{g}$  of SiO<sub>2</sub>. C) Animals administered with 800 ng of FeSO<sub>4</sub> showed a severe neuronal loss, while D) 20  $\mu\text{g}$  of SiO<sub>2</sub>-Fe administration produced a significant intraneuronal increase in the positive signal to iron (Prussian blue staining). The images were observed to 40X magnifications. E) Average of the pixel distribution positive to iron for Prussian blue stain in the brain sections were quantified. Each bar represents the mean  $\pm$  S.E.M. of 3–4 animals by group. \*P = 0.003. ANOVA followed by Tukey test.

(compared to the FeSO<sub>4</sub> treatment). The same images provide evidence that in this group there is presence of both pyknotic nuclei and surrounding macrophages in the injured area (Fig. 5D). These results support the notion that the formation of iron accumulations inside neurons through the employment of nanostructured materials of SiO<sub>2</sub> occluded with FeSO<sub>4</sub> (Fig. 5D) is efficient and an

underlying cause for the initial signs of neuronal apoptosis and neuroinflammation, a significantly milder reaction to the direct injection of  $\text{FeSO}_4$ . In Fig. 5E, we show the average distribution of iron-positive pixels in the different groups, where a significant increase ( $P = 0.003$ ) in the iron-positive signal is evident in the group administered with  $\text{SiO}_2\text{-Fe}$ . The images were analyzed using the “ImageJ/Analyze Particles” software, configured to select the blue color between pixels 40–90. Preliminary assays of iron quantification showed that the microinjection of 20  $\mu\text{g}$  of  $\text{SiO}_2\text{-Fe}$  in the *SNpc* gives place to an increase of 40% of the iron in the ventral midbrain versus the control group (data not shown).

### 3.4. Lipid peroxidation

Fluorescent lipidic product formation was evaluated from the ventral midbrain in all groups as a short-term damage marker in the *SNpc* to corroborate histological findings. The control group injected intranigrally with PBS provided information on the basal level of lipid peroxidation showing  $2.07 \pm 0.09$  fluorescent lipidic product units/ $\mu\text{g}$  of protein (Fig. 6).  $\text{SiO}_2$  intranigral administration did not produce significant changes in the fluorescent lipidic product formation at  $2.24 \pm 0.27$  fluorescent units/ $\mu\text{g}$  protein. When the animals were administrated the  $\text{FeSO}_4$  infusion a statistical increase ( $P = 0.001$ ) in the generation of fluorescent lipidic products at  $3.34 \pm 0.23$  fluorescent units/ $\mu\text{g}$  protein was observed and considered a product of lipid peroxides formed in the *SNpc* perilesional area. Nevertheless, levels of lipid peroxidation may have already decreased from a prior maximum value due to the loss of tissue at the 72 h mark. The effect of intranigral microinjection of  $\text{SiO}_2\text{-Fe}$  also generated a significant increase ( $P = 0.0461$ ) versus the control group in the formation of lipid peroxidation ( $2.84 \pm 0.07$  fluorescent units/ $\mu\text{g}$  protein), still at an intermediate value below that observed in the group treated with  $\text{FeSO}_4$ .

### 3.5. Circling behavior

A behavioral evaluation of the injected animals was carried out 6 days after surgery. We used classical assays from Norman et al. in 1990 [31] to evaluate the longer term effect of nanostructured material administration on circling behavior of the rat following apomorphine administration. As shown in Fig. 7,  $\text{FeSO}_4$  administration produced a significant ( $P = 0.001$ ) effect on circling behavior ( $232 \pm 31$  ipsilateral turns/h) against the animals administrated with PBS (control group) ( $4 \pm 1$  ipsilateral turns/h). The animal group treated with intranigral microinjection of  $\text{SiO}_2$  presented a non-significant change in the phenotype ( $31 \pm 6$  ipsilateral turns/h) in comparison with the control group, whereas  $\text{SiO}_2\text{-Fe}$  administration showed  $73 \pm 6$  ipsilateral turns/h, which represented significant differences to all other groups ( $P = 0.01$ ) once again showing an intermediate phenotype between the dramatic effect of injecting free iron and the minor disturbances of iron-free silica injection.

## 4. Discussion

Iron is an essential element and micronutrient for the central nervous system, participating in myelin formation, catecholamine metabolism, mitochondrial oxidative phosphorylation, among numerous other physiological processes [32]. Alterations in iron metabolism are closely related to neurodegenerative diseases such as Parkinson’s disease (PD), Alzheimer’s disease (AD), Huntington’s disease (HD), and amyotrophic lateral sclerosis (ALS) [33,34]. In idiopathic PD, it should be considered that the increase in iron content – identified by parenchyma brain sonography – represents a marker of neuronal damage, clinically indicated for high specificity and high diagnosis sensitivity [22]. For several decades, the main neurochemical characteristics of PD have been reproduced through various models in laboratory animals. The administration of neurotoxins such as 1-methyl-4-phenyl-1,2,3,6 tetrahydropyridine (MPTP), 6-hydroxydopamine (6-OHDA), rotenone and paraquat in rodents induce oxidative stress due to free radicals’

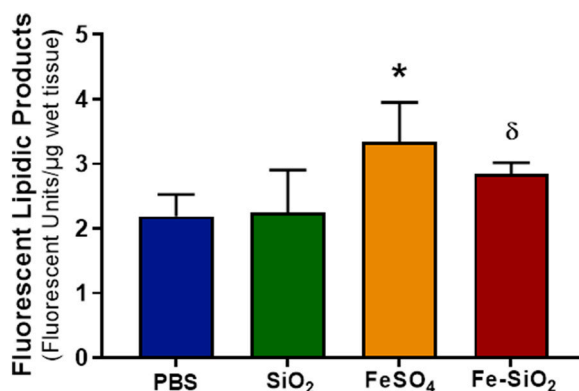


**Fig. 6.** Nanostructured material microinjection of  $\text{SiO}_2$  occluded with iron-induced lipid peroxidation in the midbrain. Both groups of animals treated with  $\text{FeSO}_4$  and  $\text{Fe-SiO}_2$  showed significant oxidative damage versus the control groups (PBS and  $\text{SiO}_2$ ). Lipid peroxidation was measured as an index of fluorescent lipidic products formation. Each bar represents the mean  $\pm$  S.E.M. of 5–7 animals. (\* $P = 0.001$  and  $\delta P = 0.046$ ) in fluorescence arbitrary units. ANOVA followed by Dunnett’s multiple comparisons test.

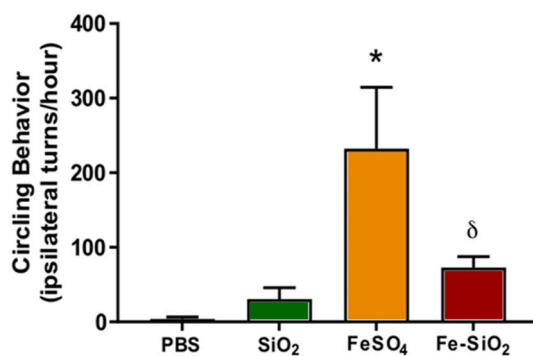


**Fig. 7.** Nanostructured materials and iron administration effects on apomorphine-induced circling behavior. Animals were evaluated six days after lesions induced both by PBS, FeSO<sub>4</sub> or nanostructured material. The rats received apomorphine and ipsilateral turns were recorded for 60 min. Results are shown as mean  $\pm$  S.E.M. from 5 to 7 rats per group. Differences from FeSO<sub>4</sub>- and SiO<sub>2</sub>-Fe-treated versus control group are shown, \* $P = 0.001$  and  $^{\delta}P = 0.01$ , respectively; data were analyzed by Kruskal–Wallis’ test followed by Dunn’s test.

overproduction, which it is accompanied by lipid peroxidation and mitochondrial damage [35]; however, these animal models of PD do not induce iron accumulation as an early marker of damage *per se*, which also does not reflect the imbalance in other transition metals, such as copper (Cu<sup>2+</sup>), zinc (Zn<sup>2+</sup>) and manganese (Mn<sup>2+</sup>) [36].

The nanostructured materials of silica dioxide occluded with ferrous sulfate used in this study have been synthesized and characterized to obtain a gradual and sustained iron release system per unit of time, which can facilitate the release of iron to the extracellular space and eventually its internalization in the neuron. The administration of 20  $\mu$ g of SiO<sub>2</sub>-Fe in the ventral midbrain of rats resulted in a substantial increase in the total iron content reproducing a marker of neuronal damage observed in patients with PD [37]. Several mechanisms have been reported by which neurons internalize iron from interstitial fluid [38]. Once iron is released from nanostructured materials, it can join transferrin [39] or lactoferrin [40] in the interstitial fluid, and subsequently, the proteins can be coupled to receptors for transferrin (Tf-TfR1) or lactoferrin (Lf-LfR1) on the neuronal membrane and be internalized by endocytosis [38]. Another iron internalization pathway happens through the divalent metal transporter-1 (DMT1), despite, the ferric reductases involved in reducing Fe<sup>3+</sup> to Fe<sup>2+</sup> have not yet been firmly identified [38]. Intraneuronal accumulation of iron deleterious effect presents a resulting production of free radicals through Fenton chemistry ( $\text{H}_2\text{O}_2 + \text{Fe}^{2+} \rightarrow \text{-OH} + \text{•OH} + \text{Fe}^{3+}$ ). Oxidative stress could also result from deficits in metal removal [36] and concomitant neural death by ferroptosis [41], consistent with the overproduction of fluorescent lipid products and the concomitant evidence of tissue and cytostructural alterations, as well as possible microglia activation or infiltrating macrophages presence in the injured zone. Indeed, an increase in cellular iron has been discussed as the possible cause of the deficit both in the antioxidant response and in the decrease in the mitochondrial electron transport chain activity [42,43], as well as glia activation [41].

On the other hand, oral iron supplementation in the form of ferrous sulfate has been evaluated as a therapeutic alternative to treat iron deficiency anemia, with no reports of adverse effects on the organism due to the increase in sulfate ions [44]. Likewise, in rats, copper sulfate administration reverted striatal and midbrain damage induced by injections of 1-methyl-4-phenylpyridinium ions, which would be an unlikely outcome if sulfate ions presented toxicity at the concentrations used [45]. Therefore, there are no indications at present that sulfate ions can cause a toxicity problem to the brain tissue, but future work should be directed to address specifically this concern. In subsequent trials, we will evaluate the possibility of additional effects of the sulfate counter ions on iron-associated neurotoxicity in the present paradigm.

In relation to the effect of apomorphine systemic administration indicated as an agonist of dopaminergic receptors of type D2 preferentially [46] induced ipsilateral turning behavior in the groups of animals treated intranurally with FeSO<sub>4</sub> or SiO<sub>2</sub>-Fe, leaving the hemisphere supersensitive to apomorphine action [28,29]. Therefore, the possible increase in receptor density could be explained by sensitization to dopamine generated after SNpc neurons degeneration. Consequently, the striatum afferent neurons become sensitized to the lack of dopamine and increase the externalization of their dopaminergic receptors [47]. Then, the contralateral normosensitive hemisphere is observed to determine this behavior produced by increase of iron [31].

Finally, the present work reports on the synthesis and characterization of SiO<sub>2</sub>-Fe nanostructured materials as well as on their application to generate neuronal damage due to intraneuronal iron accumulation in the rat SNpc, behavioral, histological, and neurochemical levels are very promising. The strategy to generate intraneuronal increase in iron opens the possibility, to analyze the time course of iron increase in the SNpc through the analysis of the change in concentrations of transition metals mentioned above (Cu, Zn, Mn) allowing the study of the early change in the expression of proteins involved in the transport and storage of iron and other transition metals. In the same way, it will be possible to evaluate the consequences of drug administration with therapeutic potential to reduce the iron content within neurons affected by the imbalance in transition metals and increase the half-life of remnant dopaminergic neurons.

## 5. Conclusion

Nanostructured SiO<sub>2</sub>-Fe material was successfully obtained by the sol-gel process. The spectroscopic results indicate that FeSO<sub>4</sub> addition to the silica network during its preparation did not cause structural or chemical changes to the iron source. Sustained release of iron was observed during the first 10 h tested *in vitro* and after 72 h *in vivo*, the biological effect of iron evaluated in the ventral midbrain of rat. Injection of the nanostructured materials of SiO<sub>2</sub>-Fe in the mesencephalic midbrain produced intraneuronal deposits of iron, histological damage, lipid peroxidation and behavioral alterations, suggesting a viable technique for inducing an intraneuronal increase of iron content and reproducing markers of damage related to neurodegenerative diseases associated with increased iron content.

The present study sets the ground to generate a model of PD through the slow increase of iron concentrations in the SNpc of the rat. Future perspectives (present limitations) include further tests to quantify the increase in iron in the brain nuclei and assays to evaluate immediate downstream effect. In the first instance, we propose to investigate the activity of complex I of the mitochondrial, evaluate the ratio of oxidized/reduced glutathione (GSH/GSSG), measure dopamine levels in the striatum of the rat and quantify dopaminergic neuronal death of the nigro-striatum pathway. It is also crucial to evaluate the effect of SiO<sub>2</sub>-Fe administration on the immune response, and on the structure of  $\alpha$ -syn. All of the above, with the prospect of challenging pharmacologically the effect of slowly accumulating iron to discover therapeutic alternatives capable of reducing the high content of the metal in the SNpc of patients with idiopathic PD and in this way promoting an increase in the half-life of dopaminergic neurons affected by the imbalance in the content of transition metals.

## Data availability statement

The raw data supporting the conclusions of this manuscript will be made available on request to any researcher in: <https://drive.google.com/drive/u/0/folders/1RuJAUahwKUZB11dAUqsnUcMgiO3uKMh8>.

## Funding statement

This work was supported by the National Council of Science and Technology, Mexico (CONACYT, Mex.) [grant number 287959], also was partially supported by the National Institute of Neurology and Neurosurgery [Protocol 24/16].

## CRediT authorship contribution statement

**E. Ortiz-Islas:** Writing – original draft, Methodology, Investigation, Formal analysis, Data curation. **A.A. Ponce-Juárez:** Methodology, Investigation, Data curation. **F. Tzompantzi-Morales:** Methodology, Formal analysis, Data curation. **M.E. Manríquez-Ramírez:** Methodology, Investigation. **C. Rubio:** Writing – review & editing, Writing – original draft, Methodology, Formal analysis, Data curation. **M. Calvillo-Velasco:** Methodology, Investigation. **G. Chávez-Cortes:** Methodology, Formal analysis, Data curation. **F. Missirlis:** Writing – review & editing, Investigation. **M. Rubio-Osornio:** Writing – review & editing, Writing – original draft, Supervision, Project administration, Methodology, Investigation, Funding acquisition, Formal analysis, Data curation, Conceptualization.

## Declaration of competing interest

The authors declare the following financial interests/personal relationships which may be considered as potential competing interests: Moises Rubio-Osornio reports financial support, article publishing charges, equipment, drugs, or supplies, and travel were provided by National Council of Science and Technology (CONACYT), Mexico. If there are other authors, they declare that they have no known competing financial interests or personal relationships that could have appeared to influence the work reported in this paper.

## Acknowledgments

Ponce-Juárez A. A. is a Doctoral student from Programa de Doctorado en Ciencias Biomédicas, Universidad Nacional Autónoma de México (UNAM) and received fellowship 1101609 from CONACYT. Also, we would like to thank the MD. Betsabet Rivero Celaya and the Dra. Daniela Silva-Adaya for their technical support in the development of this study.

## References

- [1] C. Agustin Saenza, J.A. Sanchez Garcia, M. Machado, M. Brizuela, O. Zubillaga, A. Tercjak, Broadband antireflective coating stack based on mesoporous silica by acid catalyzed sol-gel method for concentrated photovoltaic application, *Sol. Energy Mater. Sol. Cell.* 186 (2018) 154–164.
- [2] J.L. Gurav, I.K. Jung, H.H. Park, E.S. Kang, D.Y. Nadargi, Silica aerogel: synthesis and applications, *J. Nanomater.* 409310 (2010) 1–11.
- [3] M. Jafarzadeh, I.A. Rahman, C.S. Sipaut, Synthesis of silica nanoparticles by modified sol-gel process: the effect of mixing modes of the reactants and drying techniques, *J. Sol. Gel Sci. Technol.* 50 (2009) 328–336.
- [4] B. Priyanka, D. Sen, S. Mazumder, J.S. Melo, C.B. Basak, D. Kinshuk, Porous nano-structured micro-granules from silica-milk bi-colloidal suspension: synthesis and characterization, *Colloids Surf., B* 154 (2017) 421–428.
- [5] K.C. Dixit, S. Bhakta, A. Kumar, S.L. Suib, J.F. Rusling, Fast nucleation for silica nanoparticle synthesis using a sol-gel method, *Nanoscale* 8 (2016) 19662–19667.

- [6] J. Zhang, Y. Ma, F. Shi, L. Lequan, Y. Deng, Room temperature ionic liquids as templates in the synthesis of mesoporous silica via a sol-gel method, *Microporous Mesoporous Mater.* 119 (2009) 97–103.
- [7] G.J. Owens, R.K. Singh, F. Foroutan, M. Alqaysi, C.M. Han, C. Mahapatra, H.W. Kimb, J.C. Knowles, Sol-gel based materials for biomedical applications, *Prog. Mater. Sci.* 77 (2016) 1–79.
- [8] S. Maher, T. Kumeria, A.M. Sin, D. Losic, Diatom silica for biomedical applications: recent progress and advances, *Adv. Healthcare Mater.* 7 (2018) 1–19.
- [9] Y. Chen, H. Chen, J. Shi, Delivery/imaging multifunctionality of mesoporous silica-based composite nanostructures, *Exp. Opin. Drug Deliv.* 11 (2014) 917–930.
- [10] N.Ž. Knežević, D. Jean-Olivier, Large pore mesoporous silica nanomaterials for application in delivery of biomolecules, *Nanoscale* 7 (2015) 2199–2209.
- [11] T. Andreani, A.M. Silva, E.B. Souto, Silica-based matrices: state of the art and new perspectives for therapeutic drug delivery, *Biotechnol. Appl. Biochem.* 62 (2015) 754–764.
- [12] A. Bitar, A.M. Nasir, F. Hatem, A. Elaissari, Silica-based nanoparticles for biomedical applications, *Drug Discov. Today* 17 (2012) 1147–1154.
- [13] A. Karunya, H. Xin-Chun, H. Hsin-Yun, Bio-templated silica composites for next-generation biomedical applications, *Adv. Colloid Interface Sci.* 249 (2017) 272–289.
- [14] T.T. Hoang-Thi, V.D. Cao, T.N. Quynh-Nguyen, D.T. Hoang, V.D. Cuong-Ngo, H. Nguyen, Functionalized mesoporous silica nanoparticles and biomedical applications, *Mater. Sci. Eng., C* 99 (2019) 631–656.
- [15] M. Arruebo, M. Galán, N. Navascués, C. Téllez, C. Marquina, M.R. Ibarra, J. Santamaría, Development of magnetic nanostructured silica-based materials as potential vectors for drug-delivery applications, *Chem. Mater.* 18 (2006) 1911–1919.
- [16] M.S. Aw, S. Simovic, Y. Yu, J. Addai-Mensah, D. Losic, Porous silica microshells from diatoms as biocarrier for drug delivery applications, *Powder Technol.* 223 (2012) 52–58.
- [17] A. García-Fernández, E. Aznar, R. Martínez-Máñez, F. Sancenón, New advances in in vivo applications of gated mesoporous silica as drug delivery nanocarriers, *Small* 16 (2020) 1–62.
- [18] Y. Wang, Q. Zhao, N. Han, L. Bai, J. Li, J. Liu, E. Che, L. Hu, Q. Zhang, T. Jiang, S. Wang, Mesoporous silica nanoparticles in drug delivery and biomedical applications, *Nanomed. Nanotechnol. Biol. Med.* 11 (2015) 313–327.
- [19] S.C. Moorcroft, D.G. Jayne, S.D. Evans, Z.Y. Ong, Stimuli-responsive release of antimicrobials using hybrid inorganic nanoparticle associated drug-delivery systems, *Macromol. Biosci.* 18 (2018) 1–14.
- [20] M. Rubio-Osornio, M. Orozco-Ibarra, A. Díaz-Ruiz, E. Brambila, M.C. Boll, A. Monroy-Noyola, J. Guevara, S. Montes, C. Ríos, Copper sulfate pretreatment prevents mitochondrial electron transport chain damage and apoptosis against MPP+ induced neurotoxicity, *Chem. Biol. Interact.* 271 (2017) 1–8.
- [21] M. Ozansoy, A.N. Başak, The central theme of Parkinson's disease:  $\alpha$ -synuclein, *Mol. Neurobiol.* 47 (2013) 460–465.
- [22] U. Walter, L. Niehaus, T. Probst, R. Benecke, B.U. Meyer, D. Dressler, Brain parenchyma sonography discriminates Parkinson's disease and atypical parkinsonian syndromes, *Neurology* 60 (2003) 74–77.
- [23] N.P. Parameswaran, M.V. Sudha, S.A. Kumar, V. Harikrishna, High surface area sol-gel nano silica as a novel drug carrier substrate for sustained drug release, *Mater. Res. Bull.* 47 (2012) 1379–1384.
- [24] A.Ü. Düzlü, B. Günaydn, M.K. Şüküröglü, İ.T. Değim, Release pattern of liposomal bupivacaine in artificial cerebrospinal fluid, *Turkish Journal of Anaesthesiology & Reanimation* 44 (2016) 1–6.
- [25] G. Paxinos, C. Watson (Eds.), *The Rat Brain in Stereotaxic Coordinates*, Academic Press, New York, 1998.
- [26] J.W. Triggs, L.J. Willmore, In vivo lipid peroxidation in rat brain following intracortical  $Fe^{2+}$  injection, *J. Neurochem.* 42 (1984) 976–980.
- [27] O.H. Lowry, N.J. Rosebrough, A.L. Farr, R.J. Randall, Protein measurement with the folin-phenol reagent, *J. Biol. Chem.* 193 (1951) 265–275.
- [28] M. Rubio-Osornio, S. Montes, Y. Heras-Romero, C. Rubio, Y. Rivera-Mancia, E. Floriano-Sánchez, J. Guevara, C. Ríos, Induction of ferroxidase enzymatic activity by copper reduces neurotoxicity MPP+ evoked in rats, *Neurosci. Res.* 75 (2013) 250–255.
- [29] D. Trivedi, S. Jana, Solid state characterization of the consciousness energy healing treated ferrous sulphate, *Journal of Nutrition and Health Sciences* 6 (2019) 1–9.
- [30] E. Ortiz-Islas, A. Sosa-Arróniz, M.E. Manríquez-Ramírez, C.E. Rodríguez-Pérez, F. Tzompantzi, J.M. Padilla, Mesoporous silica nanoparticles functionalized with folic acid for targeted release Cis-Pt to glioblastoma cells, *Rev. Adv. Mater. Sci.* (2021) 6025–6037.
- [31] A.B. Norman, L.M. Wyatt, J.P. Hildebrand, M. Kolmonpunpörn, C.A. Moody, M.N. Lehman, P.R. Sanberg, Sensitization of rotation behavior in rats with unilateral 6-hydroxydopamine or kainic acid-induced striatal lesions, *Pharmacol. Biochem. Behav.* 37 (1990) 755–759.
- [32] A. Thirupathi, Y. Chang, Brain iron metabolism and CNS diseases, *Adv. Exp. Med. Biol.* 1173 (2019) 1–19.
- [33] S. Chen, Y. Chen, Y. Zhang, X. Kuang, Y. Liu, M. Guo, Iron metabolism and ferroptosis in epilepsy, *Front. Neurosci.* 14 (2020) 601193.
- [34] S. Rivera-Mancia, I. Pérez-Neri, C. Ríos, L. Tristán-López, L. Rivera-Espinosa, S. Montes, The transition metals copper and iron in neurodegenerative diseases, *Chem. Biol. Interact.* 186 (2010) 184–199.
- [35] S.A. Jagmag, N. Tripathi, S.D. Shukla, S. Maiti, S. Khurana, Evaluation of models of Parkinson's disease, *Front. Neurosci.* 19 (9) (2016) 1–13.
- [36] L. Mezzaroba, D.F. Alfieri, A.N. Colado-Simão, E.M. Vissoci-Reiche, The role of zinc, copper, manganese and iron in neurodegenerative diseases, *Neurotoxicology* 74 (2019) 230–241.
- [37] F.A. Zucca, J. Segura-Aguilar, E. Ferrari, P. Muñoz, I. Paris, D. Sulzer, T. Sarna, L. Casella, L. Zecca, Interactions of iron, dopamine and neuromelanin pathways in brain aging and Parkinson's disease, *Prog. Neurobiol.* 155 (2017) 96–119.
- [38] S.R. D'Mello, M.C. Kindy, Overdosing on iron: elevated iron and degenerative brain disorders, *Exp. Biol. Med.* 245 (2020) 1444–1473.
- [39] T. Moos, T.N. Rosengren, T. Skjörninge, E.H. Morgan, Iron trafficking inside the brain, *J. Neurochem.* 103 (2007) 1730–1740.
- [40] J.H. Brock, Lactoferrin-50 years on, *Biochem. Cell. Biol.* 90 (3) (2012) 245–251.
- [41] W. Zhang-Li, Y. Lin, L. Wen, L. Jia-Yi, Ferroptosis in Parkinson's disease: glia-neuron crosstalk, *Trends Mol. Med.* 28 (2022) 258–269.
- [42] I.C. Lavich, B.S. de Freitas, L.W. Kist, L. Falavigna, V.A. Dargél, L.M. Köbe, C. Aguzzoli, B. Piffero, P.Z. Florian, M.R. Bogo, M.N. de Lima, Sulforaphane rescues memory dysfunction and synaptic and mitochondrial alterations induced by brain iron accumulation, *Neuroscience* 1 (2015) 542–552.
- [43] X. Shuang-Feng, Z. Yan-Hui, W. Shan, P. Zhong-Qiu, F. Yong-Gang, Lactoferrin ameliorates dopaminergic neurodegeneration and motor deficits in MPTP-treated mice, *Redox Biol.* 21 (2019) 101090.
- [44] U.N. Stoffel, C.I. Cercamondi, G. Brittenham, C. Zeder, A.J. Geurts-Moespot, D.W. Swinkels, D. Moretti, M.B. Zimmermann, Iron absorption from oral iron supplements given on consecutive versus alternate days and as single morning doses versus twice-daily split dosing in iron-depleted women: two open-label, randomised controlled trials, *Lancet Haematol* 4 (2017) 524–533.
- [45] M. Islas-Cortez, C. Ríos, M. Rubio-Osornio, S. Zamudio, S. Orozco-Suarez, M. Mendez-Armenta, C. Nava-Ruiz, A. Diaz-Ruiz, Characterization of the antiapoptotic effect of copper sulfate on striatal and midbrain damage induced by MPP+ in rats, *Neurotoxicology* 82 (2021) 18–25.
- [46] S. Giménez-Roldán, S. García-Muñozguren, Use of apomorphine in Parkinson's disease, *Rev. Neurol.* 35 (2002) 668–674.
- [47] P.A. Caro Aponte, C.A. Otálora, J.C. Guzmán, L.F. Turner, J.P. Alcázar, E.L. Mayorga, Correlation between dopamine receptor D2 expression and presence of abnormal involuntary movements in Wistar rats with hemiparkinsonism and dyskinesia, *Neurologia* 36 (3) (2021) 191–200.